Volume 15
Number 47
21 December 2023
Pages 18945-19392

Nanoscale

rsc.li/nanoscale

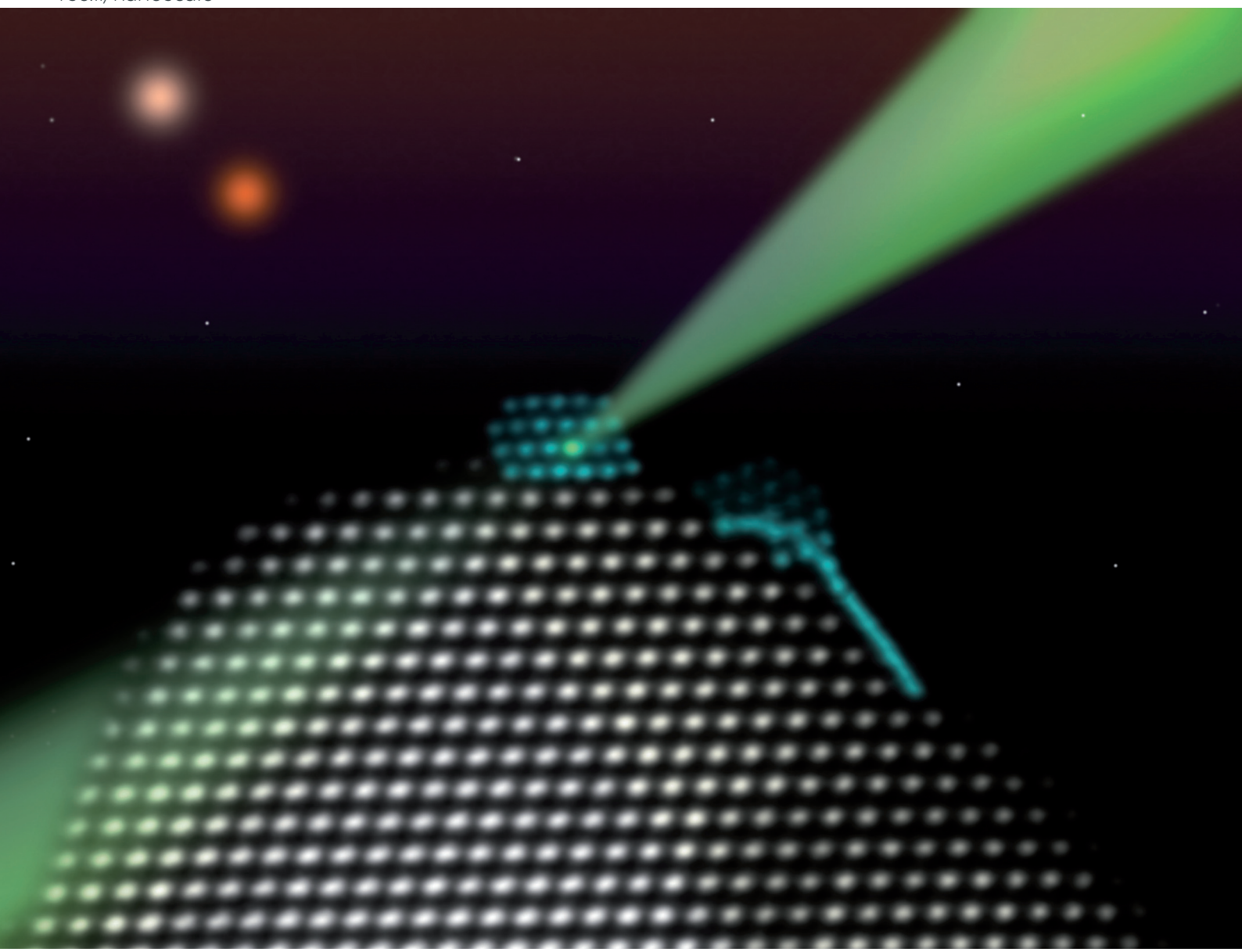

ISSN 2040-3372

ROYAL SOCIETY OF CHEMISTRY

PAPER
Rolf Erni *et al.*
Support-facet-dependent morphology of small Pt particles on ceria

NCNST

Nanoscale

PAPER

View Article Online
View Journal | View Issue

Cite this: *Nanoscale*, 2023, **15**, 19091

Support-facet-dependent morphology of small Pt particles on ceria†

Henrik Eliasson, [a] Yubiao Niu,[b] Richard E. Palmer, [b] Henrik Grönbeck [c] and Rolf Erni *[a,d]

Received 18th September 2023,
Accepted 31st October 2023

DOI: 10.1039/d3nr04701f

rsc.li/nanoscale

Direct atomic scale information on how the structure of supported nanoparticles is affected by the metal–support interaction is rare. Using scanning transmission electron microscopy, we provide direct evidence of a facet-dependent support interaction for Pt nanoparticles on CeO_2, governing the dimensionality of small platinum particles. Our findings indicate that particles consisting of less than ~130 atoms prefer a 3D shape on CeO_2(111) facets, while 2D raft structures are favored on CeO_2(100) facets. Measurements of stationary particles on both surface facets are supplemented by time resolved measurements following a single particle with atomic resolution as it migrates from CeO_2(111) to CeO_2(100), undergoing a dimensionality change from 3D to 2D. The intricate transformation mechanism reveals how the 3D particle disassembles and completely wets a neighboring CeO_2(100) facet. Density functional theory calculations confirm the structure-trend and reveal the thermodynamic driving force for the migration of small particles. Knowledge of the presented metal–support interactions is crucial to establish structure–function relationships in a range of applications based on supported nanostructures.

Introduction

Understanding how clusters and nanoparticles are affected by their local environment is key to optimizing particle-based functional materials. Free-standing metal nanoparticles are usually expected to adopt icosahedral, decahedral or octahedral shape, as predicted by the Wulff theorem.[1,2] However, nanoparticles are not free-standing in most applications, and thus a range of factors must be taken into account to predict the structure and thereby properties of a supported particle. Considering a small metal particle on a metal–oxide surface, some key factors for the structural prediction are particle size,[3] surface energy of the particle and of the support facet,[2] geometry of the interface,[4] and chemical environment.[5–7] Adding metal–support interactions (MSI) into computational studies increases the computational complexity significantly, and a substantial number of stable particle structures could be envisioned. Experimental data in the form of direct observations could reduce the number of theoretically possible structures to the most relevant ones. Still, direct observations showing atomically resolved structural information of both particle and support are scarce,[8–10] and even rarer is experimental data on how a single particle is affected by different supporting facets.

Scanning transmission electron microscopy (STEM) is a standard technique for analysis of nanostructured materials. The mass-thickness contrast and the incoherent nature of the high-angle annular dark-field (HAADF) signal yields directly interpretable high resolution STEM (HR-STEM) data, and is especially suited for material systems where the active phase has a larger atomic number than the support, as is the case for many materials used in heterogeneous catalysts.[11–13] With modern detectors and aberration corrected microscopes, it is possible to acquire HAADF-STEM data with a spatial resolution of less than 50 pm at several frames per second.[14,15] In order to utilize the full potential of STEM and extract three-dimensional information about a nanostructure, there are in principle three possible approaches: tomography,[16–18] depth sectioning,[19] and atom counting.[20–22] Due to the small electron dose needed, atom counting is the most suitable approach when studying small and sensitive surface-supported nanostructures that behave dynamically. The technique is based on post-processing of experimental images followed by analysis of the pixel intensities of imaged atomic columns to statistically estimate the number of atoms in the depth of each column. Arranging the number of atoms according to a lattice then yields a rough 3D model of the imaged nanostructure.

[a]*Electron Microscopy Center, Empa – Swiss Federal Laboratories for Materials Science and Technology, Überlandstrasse 129, 8600 Dübendorf, Switzerland. E-mail: rolf.erni@empa.ch*
[b]*Nanomaterials Lab, Faculty of Science and Engineering, Swansea University, Bay Campus, Swansea, SA1 8EN, UK*
[c]*Department of Physics and Competence Centre for Catalysis, Chalmers University of Technology, SE-41296 Göteborg, Sweden*
[d]*Department of Materials, ETH Zurich, CH-8093 Zurich, Switzerland*
† Electronic supplementary information (ESI) available. See DOI: https://doi.org/10.1039/d3nr04701f

To verify the validity of the proposed structure, STEM image simulations of the estimated structure can be directly compared with experimental data.[23–25]

Platinum particles supported on cerium dioxide is a widely studied material system, commonly used as an oxidation catalyst.[26–29] The relevant Pt particle size in catalyst applications is generally below 5 nm, and particles up to a few hundred atoms are attracting most attention.[26–28,30–32] Recently, two-dimensional (2D) Pt particles and ways to promote their formation have been discussed in literature.[28,33–36] These structures have been reported to have favorable catalytic properties, especially for low temperature CO oxidation, which is a reaction of high technological relevance.[28,35] The reason why 2D structures are measured to have a higher activity than 3D structures is not fully understood, however one speculation is that planar structures increase the Pt/ceria interface, which could be beneficial for low-temperature CO oxidation *via* a Mars–van Krevelen reaction path.[37,38] Considering the large difference in surface energy[39] and reported performance of CeO_2(100) and CeO_2(111) facets,[40,41] the question arises whether the corresponding support interactions would be sufficiently strong to modify the structural preference for supported nanostructures.

In this work, we utilize time-resolved atomic-resolution STEM imaging to unravel support-facet-dependent effects on the structure and morphology of platinum nanoparticles on CeO_2. We generate realistic atomic models of observed particle structures and estimate their stability by density functional theory (DFT) calculations. Moreover, a particle is monitored with atomic resolution as it migrates from CeO_2(111) to CeO_2(100). We observe a structural transformation in the particle from a 3D shape to a 2D shape as the particle moves from CeO_2(111) to CeO_2(100) and we discuss the implications of, mechanisms within, and causes behind, the transformation.

Results

The comprehensive high resolution HAADF-STEM study of size-selected Pt_{130} particles deposited by the cluster beam technique[42] onto CeO_2, reveals a dynamic particle behavior. Platinum particles on CeO_2(111) were found in several orientations with respect to the support, with a slight preference for the alignment of the ⟨110⟩ zone axes of the support and particle, which is in agreement with previous reports.[8,9] In all cases where the crystal structure of the Pt particle is visible, and thus well aligned to the electron beam, we can identify that the interface between particle and support is Pt(111) on CeO_2(111). The (111) facet is the stable facet for both Pt and CeO_2 and indicates a low adhesion energy.[2,39,43,44] As a result of the weak interaction, we see that Pt particles on CeO_2(111) are dynamic and transform between different 3D structures while maintaining the epitaxial relation. A representative dynamic sequence is presented in Fig. 1 (see also ESI movies 1 & 2†).

Frequently, we also detect a few ceria columns in the vicinity of observed particle-support interfaces (one example is highlighted in Fig. 1b). Such columns form a small ceria step that typically moves with the diffusing Pt particle on CeO_2(111). We exclude that the step could be Pt atoms as they fit well with the ceria lattice and never participated in the observed Pt-dynamics. For model simplicity, we also assume that there is no intermixing of Pt and Ce in the interfacial columns. DFT calculations of the structures in Fig. 2, with and without a ceria step next to the interface, show that the step only has a marginal stabilizing effect on the Pt particle. However, it is clear that the presence of the ceria columns influences the dynamics of the Pt particle and enables the formation of unusual structures like the one displayed in Fig. 1f.

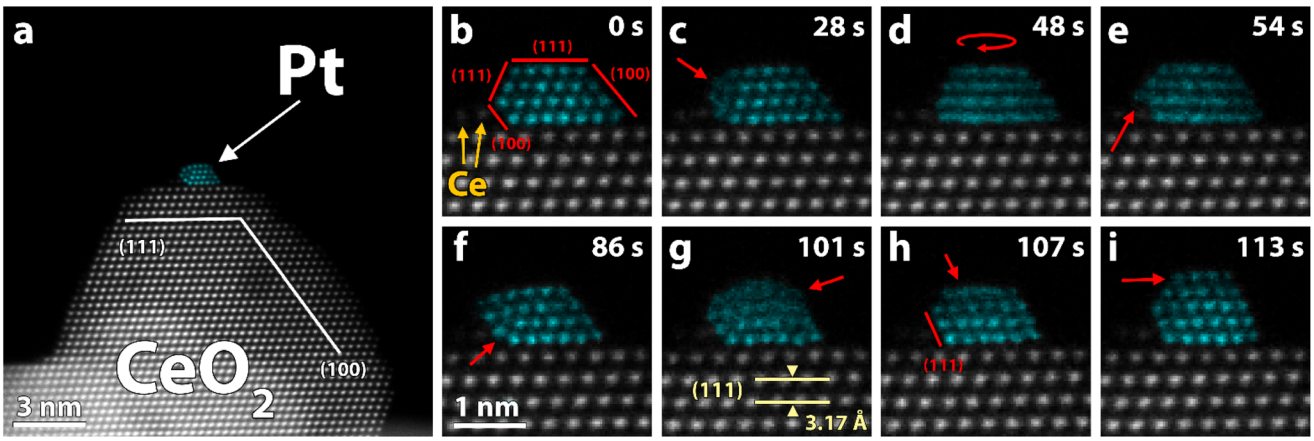

Fig. 1 HAADF-STEM images of a single platinum particle supported on CeO_2(111) in vacuum. Platinum (turquoise) has been false colored to improve visibility (grayscale version in Fig. S7†). (a) Full field-of-view of the region of interest. (b–i) Selected frames from a time series showing the dynamic behavior of the particle in (a) (full sequence in SI_mov_1†). (c) The facet facing the CeO_2-step is unstable and is restructuring. (d and e) The particle rotates and climbs on top of a CeO_2 column. (f) An intermediate quasi-stable structure where the side facing the step no longer follows the lattice of the rest of the particle. (g and h) The upper two layers are unstable and the particle tilts over to the right so that the facet facing the CeO_2-step is Pt(111) instead of Pt(100). (i) A five-layer structure is formed.

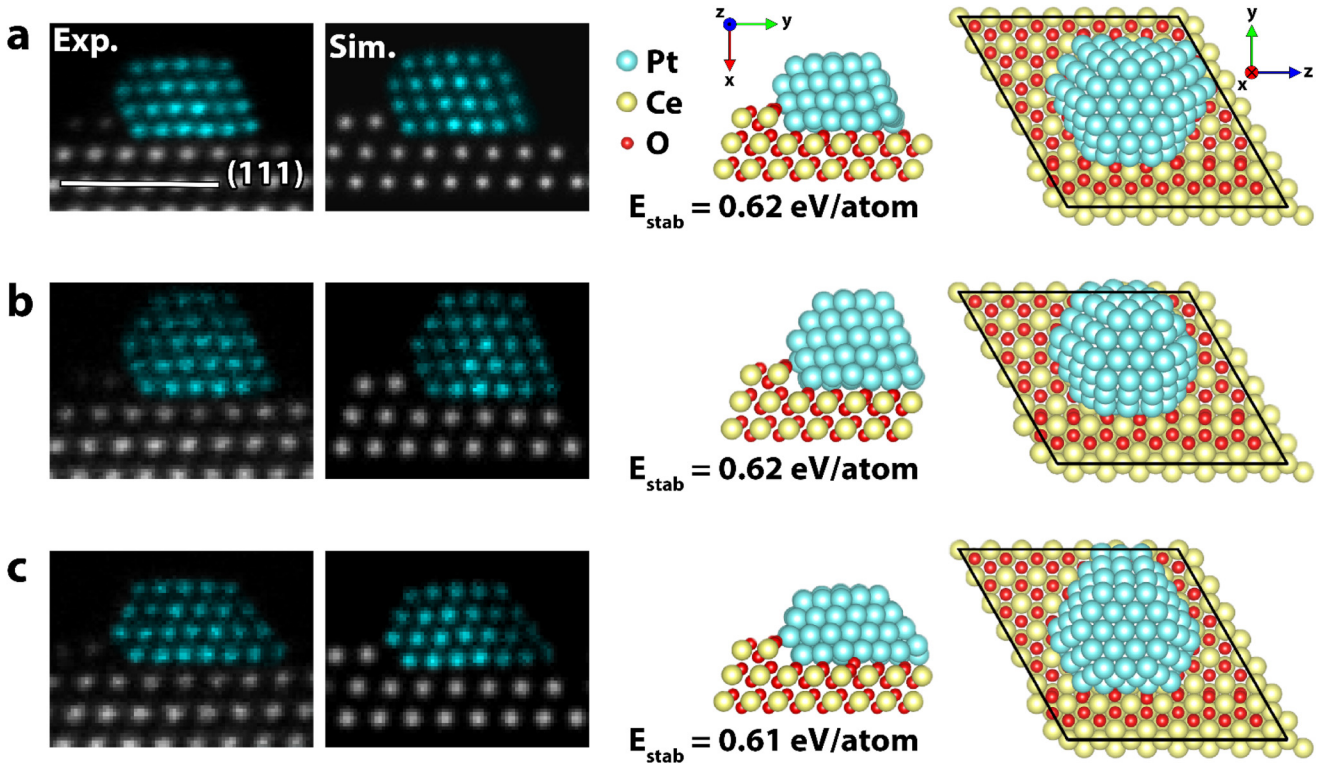

Fig. 2 (a–c) Experimental HAADF-STEM image (Exp.), simulated image (Sim.), and predicted and computationally relaxed structure (side-view and top-view) of three structures adopted by the Pt_{118} particle in Fig. 1. Despite having different structures, the three particles have similar stability. The simulated images are multi-slice STEM simulations of the predicted structures with Poisson noise applied. False color STEM images: columns identified as Pt, based on the local lattice spacing and image intensity, are plotted in turquoise (grayscale version in Fig. S8†).

We selected three stable structures, adopted by the particle in Fig. 1, and conducted further analysis to estimate particle size, stability, wetting angles and exposed facets. Based on our iterative particle analysis (see methods) we expect the particle to consist of about 118 atoms. The size-selected clusters were supposed to yield 130 atom clusters. Taking into account the accuracy of the cluster-beam deposition technique, some atoms lost on impact, and subsequent sample preparation, 118 atoms is a reasonable number. The predicted structures are presented in Fig. 2 along with corresponding experimental and simulated HAADF-STEM images. The stability of a particle structure was defined as the difference between total energy per Pt atom and Pt cohesive energy, thus a smaller value indicates a more stable structure with zero being the same stability as Pt in the bulk (see methods). For the three models in Fig. 2a, b and c, the stability was calculated to be 0.62 eV per atom, 0.62 eV per atom and 0.61 eV per atom, respectively. This can be compared to the stability of a freestanding truncated octahedron Pt_{116} that is 0.74 eV per atom. The difference in E_{stab} of the three supported particles is smaller than the thermal fluctuations per atom at room temperature, which indicates that all three structures should be present under the experimental conditions, regardless of electron irradiation, provided that the transformation barriers are small. A symmetric and ideal Pt_{119} particle inspired by the other structures was also relaxed to act as reference (Fig. S2†). Notably, this structure was calculated to be slightly less stable than the estimated particles with an E_{stab} of 0.64 eV per atom. The estimated particles exhibit only (111) and (100) facets. Regarding wetting angle, we observe no apparent trend besides the particle facet facing the ceria step generally forming an obtuse wetting angle. Otherwise, both (111) and (100) facets could be found with obtuse and acute wetting angles. A Bader charge analysis was carried out and we observe a similar charge transfer from all structures to the support, giving rise to Ce^{3+} in the ceria surface. The transfer of charge from the metal to the oxide is consistent with previous reports.[45]

Most of the observed particles are reminiscent of four-layer half truncated octahedra with a (111) base and top. The (111) side surfaces have a diameter of 5 atoms and the (100) square facets are 3 by 3 atoms. However, the structures are somewhat asymmetric as some (100) facets extend all the way down to the interface like on the right side of the structure in Fig. 1b, c and f.

The particle analyzed in Fig. 1 and 2 stayed on the CeO_2(111) facet for 95 min until it spontaneously moved to the edge of the CeO_2(111) facet and started migrating onto the neighboring CeO_2(100) facet. The observed dynamics is likely triggered by the impact of the electron beam and thus by the elastic interaction of incident electrons with Pt atoms. The particle moves initially as a 3D unit onto a (113) nanofacet of ceria where it adopts quasi-stable crystalline structures

showing a complex interface. The particle remains in this position and appears kinetically and/or thermodynamically hindered to diffuse further as one unit. Instead, single atoms start diffusing from the particle base onto the neighboring (100) facet where a 2D Pt structure forms. As the raft grows, it replaces surface ceria columns effectively reducing the size of the exposed high energy CeO_2(100) facet. Selected frames of the sequence are presented in Fig. 3. The 2D structure appeared stable during imaging and no signs of Pt atoms forming a second Pt layer were observed. To elucidate the migration, the stability of Pt_{37} on CeO_2(111) and CeO_2(100), representing the initial and final state of the experimental observation, was investigated. The Pt_{37} particle was selected to reduce the computational load, and it was relaxed on the two facets in both 3D and 2D configurations. The initial 3D structure was derived from the core of the larger Pt_{118} particle. The CeO_2(100) surface was considered to be oxygen terminated with half the oxygen coverage at the surface, which is a non-polar surface.[46]

On CeO_2(111), the 3D structure is found to be preferred over the 2D structure by 5.5 eV (Fig. S3†). The reverse trend applies for CeO_2(100) where the 2D structure is preferred by 3.9 eV over the 3D structure (Fig. S4†). The most stable structure of the monolayer on CeO_2(100) is by our calculations a (111) plane with a calculated stability of 0.63 eV per atom, which is similar to the more than three times larger 3D structures in Fig. 2. In contrast, the stability of the favored 3D structure of Pt_{37} on CeO_2(111) was calculated to 0.92 eV per atom. The significantly higher value signals a strong thermodynamic driving force for migration from CeO_2(111) to CeO_2(100) for Pt_{37}. Furthermore, moving one of the atoms of the raft to form a second layer was calculated to be endothermic by 2 eV on CeO_2(100), which is in accord with the experimental observation of a stable 2D structure. Interestingly, the opposite applies for CeO_2(111), where formation of an adatom in a second layer is exothermic by 0.9 eV. It is noteworthy that a raft of the (111) plane is the favored structure despite the square symmetry of the underlying CeO_2(100). This agrees

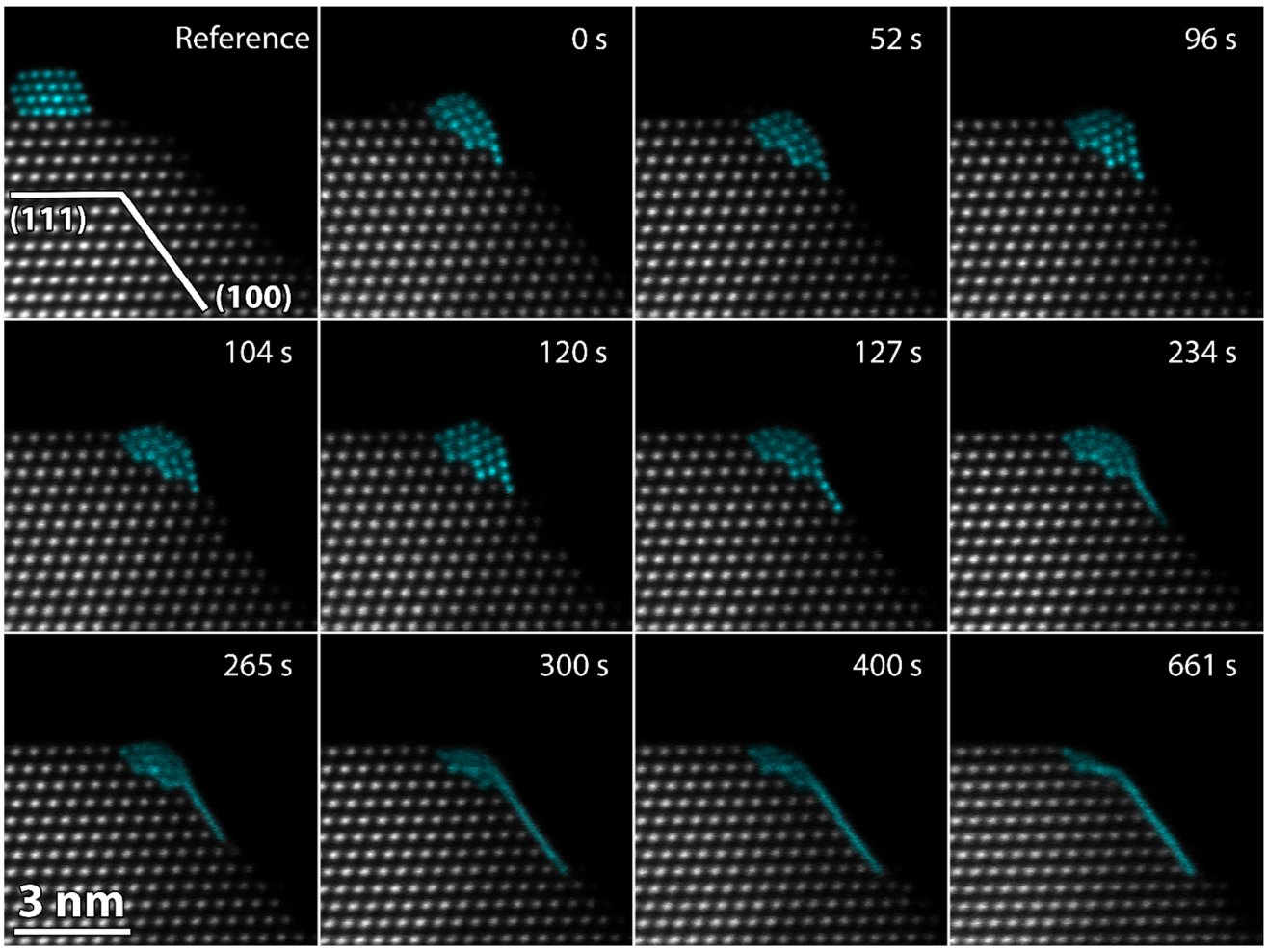

Fig. 3 HAADF-STEM time series of a platinum particle migrating from CeO_2(111) to CeO_2(100). The particle transforms from a 3D structure to a 2D structure because of the change in supporting facet. The transformation mechanism shows how single atoms diffuse from the base of the 3D particle to form a raft on the neighboring CeO_2(100) facet. The full sequence can be seen in the ESI movies (SI_mov_3 & SI_mov_4†). False color STEM images: columns identified as Pt, based on the local lattice spacing and image intensity, are plotted in turquoise (grayscale version in Fig. S9†).

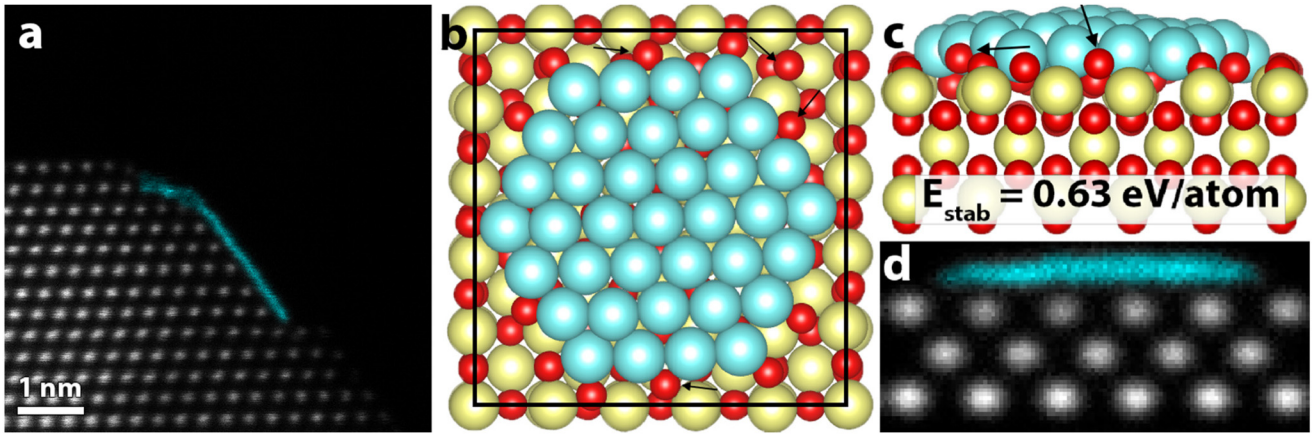

Fig. 4 (a) HAADF-STEM image of the final 2D structure. (b) Relaxed model of a Pt(111) raft on a CeO_2(100) surface. (c) Side view of (b). Black arrows point at a few examples of large structural relaxation in the CeO_2 surface oxygen anions. (d) STEM simulation of the structural model in (b) and (c), showing a similar signature as the experimental observation in (a). False color STEM image: columns identified as Pt, based on the local lattice spacing and image intensity, are plotted in turquoise (grayscale version in Fig. S10†).

with previously reported observations of non-embedded 2D Pt structures on CeO_2 that do not follow the registry of the ceria lattice.[28] The hexagonal atom arrangement in the Pt-raft gives rise to a large structural relaxation in the ceria layer, which can be seen in Fig. 4. During structural optimization, oxygen anions are relaxed to the interface of the raft.

Discussion

For three-dimensional particles about 130 atoms in size, our results show that the energy landscape of possible structures is complex, and considering thermal fluctuations, there is likely not one strictly favorable structure at room temperature. The fact that a symmetric Pt_{119} particle is less stable than an asymmetric Pt_{118} particle with very similar structure further supports this conclusion. The dynamic behavior of the 3D particles, including transformations between different structures, is likely temperature induced,[14] activated, and to some degree amplified, by the electron beam. However, we believe that for this specific material (Pt/CeO_2), and with the chosen imaging parameters, the electron beam is non-destructive and relatively gentle. This is corroborated by the fact that the particle underwent no major structural changes for a duration of more than 90 min, prior to the actual facet transition. The long exposure to electron irradiation without noticeable shrinking of the particle is not consistent with knock-on damage.[47] Furthermore, the effects of electron scattering within the sample cannot be significant if particles with fewer than 130 atoms retain a given structure for 10 s under electron irradiation, as observed in our measurements. With a short pixel dwell time in STEM imaging of down to 100 ns, we ensure that the sample only accumulates a small amount of energy and has sufficient time to relax before the beam probes the same area again. Increasing the beam current by a factor of two, or the dwell time to the microsecond-scale, introduced significant volatility in observed particle dynamics, and prevented acquisition of images with similar level of structural information as in those presented herein.

The migration sequence provides direct evidence that the facet and termination of the CeO_2 support affects the structure of supported Pt nanoparticles. As shown here, the effect can even be large enough to control the dimensionality of moderately sized species. On CeO_2(100), small Pt particles are found to be more stable as 2D rafts than as 3D particles. This was verified computationally for Pt_{37} and experimentally for Pt_{118}. Importantly, Pt_{37} on CeO_2(100) is in the calculations found to be more stable than a similarly sized 3D particle on CeO_2(111), thus there is a thermodynamic driving force for particle migration between the facets. In the experiments of Pt_{118}, the migration from CeO_2(111) to CeO_2(100) and the simultaneous structural change appeared to be irreversible, which indicates that the process is thermodynamically preferred also for this particle. Yet, with increasing Pt particle size 3D structures are expected also on CeO_2(100) because of a decreasing surface-to-bulk ratio.

The mechanism behind the transformation of the particle from 3D to 2D is peculiar. The particle, which easily diffuses as a 3D unit (*via* atomic elementary steps) on CeO_2(111), appears clamped in place with single atoms continuously diffusing away at the first point of contact with the CeO_2(100) facet. Since this sequence was only observed once, not counting particle images like Fig. S5a,† general conclusions about specific transformation steps are hard to draw. The migration is likely the product of random surface diffusion induced by temperature and electron irradiation, until contact is made with the (100) facet where the adhesion between Pt and CeO_2(100) is too strong to maintain a 3D structure. The raft then seems to grow in one plane. Although we never experimentally observe any Pt adatoms on the Pt raft, it is possible

that they are present, only rare enough and too fast moving to appear as more than noise in our data. With a temporal resolution of a few frames per second and a pixel dwell time on the order of hundreds of nanoseconds, the probability of recording a Pt adatom is low. A 300 keV electron can transfer more than the 2 eV needed[14] to generate a Pt adatom, thus they should be present, and such a mechanism could therefore contribute to the raft growth. As atoms detach, the crystalline 3D particle adopts a hemispherical shape, and it becomes increasingly disordered. At first, the growing monolayer retains the orientation of the particle with respect to the electron beam, but as it grows bigger, the Pt raft rotates, potentially to adopt a structure like the one presented in Fig. 4. This immediate dimensionality change on contact with the CeO_2(100) facet raises the question whether all small particles that migrate to CeO_2(100) will form stable 2D structures localized just at the border of the facet. This could have implications for the ageing behavior of the Pt/CeO_2 catalyst and for the desired morphology of CeO_2 to optimize the catalytic activity of the supported Pt particles.

Experimental section

Sample preparation

Catalyst model systems were prepared by Pt-cluster deposition onto a commercially available powder of 25 nm CeO_2 nanoparticles. The support powder was dispersed in methanol, ground in a mortar, and drop casted on a copper TEM-grid covered with a lacey carbon film. Size-selected Pt_{130} clusters were produced at the new Swansea Satellite Nanolab at Diamond Light Source (B07) with the cluster beam deposition technique. The cluster beam deposition source is a vacuum-based magnetron-sputtering, gas condensation source, equipped with a lateral time-of-flight mass filter.[42] The resolution of the mass filter is about 1 atom in 20, and the transmission efficiency for the selected mass is >50%. The Pt clusters were landed in high vacuum at typical kinetic energies of ~1 eV per atom, the soft-landing regime. Before insertion into the microscope, the samples were plasma cleaned in an oxygen–argon plasma for 2 rounds of 3 s.

Scanning transmission electron microscopy

The samples were analyzed at room temperature with a probe-corrected Titan Themis operated at 300 kV. The electron beam and the imaging parameters were tuned to be as non-destructive as possible while still yielding interpretable atomic resolution data. The beam convergence angle was set to nominally 17.4 mrad and the spot size was chosen such that the beam current was measured to a low value of ~20 pA. To further limit beam-effects, the pixel dwell time was set to low values between 100–500 ns, and the pixel size was never smaller than 25 pm. The electron dose in each scan is thus between 200 and 100 electrons per Å^2. Longer dwell times and larger beam currents lead to considerable volatility of the particle.

Image series were recorded at up to 10 frames per second. Frames were rigidly aligned with SmartAlign[48] and sequential frames showing the same structure were summed and averaged resulting in atomically resolved images with high signal to noise ratio. The images in Fig. 4 are the sum of 10 frames while the ones in Fig. 1b–i are the sum of 3 frames. Initial 3D-structures of the most stable observed structures were generated with StatSTEM.[49] The structures were manually tweaked to a compact structure by removing highly uncoordinated atoms and filling gaping vacancies. A STEM simulation of the resulting 3D structure was then calculated with Dr Probe[50] using a multi-slice algorithm. Poisson noise was added to the simulated image to imitate the experimental noise. After visual comparison between experimental and simulated images, the estimated 3D structures were further tweaked and their STEM image simulated again. This process was repeated until satisfactory agreement between simulated image and experimental image was achieved.

DFT calculations

Different Pt structures were relaxed on CeO_2(111) and CeO_2(100) using DFT calculations using the Vienna *ab initio* simulation package (VASP).[51–53] The valence electrons are described with a plane wave basis set using a cutoff energy of 420 eV, whereas the interaction between the valence and the core electrons is described with the projector augmented wave (PAW) method.[54] The number of valence electrons treated explicitly in the calculations are O(6), Pt(10) and Ce(12). Exchange–correlation effects are modeled using the Perdew–Burke–Ernzerhof (PBE) functional.[55] A Hubbard-U term[56] is used for Ce 4f to better describe electron localization and formation of Ce^{3+} ions in case of charge transfer from Pt. Following the literature, a *U*-value of 4.5 eV is used for Ce.[57] The surface cells are large and the *k*-point sampling is, thus, restricted to the gamma point. The electronic structure is considered to be converged when the energy difference between subsequent steps is smaller than 5×10^{-6} eV. The atomic geometries are optimized using the conjugate gradient method and the structures are considered to be converged when all forces are smaller than 5×10^{-2} eV Å^{-1}.

Different reconstructions for the CeO_2(100) surface have been proposed in literature.[46] We have chosen a structure that is 50% oxygen terminated compared to a pristine surface (Fig. S1†). Both the CeO_2(111) and the CeO_2(100) slabs are stoichiometric with the same termination on both sides. With these structures, the surface energy was calculated to be 0.72 J m^{-2} for CeO_2(111) and 1.47 J m^{-2} for CeO_2(100). The values are in agreement with previous reports using similar computational approaches.[39] The stability of a Pt particle supported on CeO_2(*hkl*) was calculated from the total DFT energies as:

$$E_{\mathrm{stab}} = \frac{1}{N}\left(E_{\mathrm{Pt/CeO_2}} - E_{\mathrm{CeO_2}(hkl)} - N \cdot E_{\mathrm{Pt(bulk)}}\right).$$

The charge distribution in the system was investigated using a Bader charge analysis.[58]

Conclusion

We have presented experimental and computational evidence that the facet-dependent support interaction in Pt/CeO_2 is strong enough (i) to control the dimensionality of moderately sized Pt particles (<2 nm) and (ii) to trigger a diffusion controlled transition of the Pt particles from the $CeO_2(111)$ to the $CeO_2(100)$ surface facet. The effect could potentially be utilized to engineer the morphology of catalytic nanoparticles in the Pt/CeO_2 system by tuning exposed surface facets of CeO_2 and platinum particle size. Platinum particles of fewer than 130 atoms form stable 2D raft structures when supported on $CeO_2(100)$ in contrast to being a mobile 3D particle when supported on $CeO_2(111)$. Our DFT calculations show that this pronounced change is directly related to the larger surface energy of $CeO_2(100)$ and the corresponding high $Pt/CeO_2(100)$ adhesion. The structure trend was confirmed by recording the migration of a single Pt particle from a 3D structure on $CeO_2(111)$ to a 2D structure on $CeO_2(100)$. The migration sequence shows how the particle stops on the ridge between the two facets and single atoms diffuse onto the $CeO_2(100)$, pushing away the surface ceria and forming a raft structure in their wake. The mechanism is attributed to the high surface energy of $CeO_2(100)$. Furthermore, the 2D structure is special in that the most stable configuration is a Pt(111) plane on $CeO_2(100)$, two non-matching geometries that in turn give rise to a large relaxation of the surface oxygen anions of CeO_2. We have also shown that 3D Pt_{118} particles on $CeO_2(111)$ are reminiscent of asymmetric half truncated octahedral, forming a Pt (111) on $CeO_2(111)$ interface. Moreover, the difference in stability of similar 3D structures is smaller than the thermal fluctuations per atom at room temperature, which indicates that under realistic conditions, and on identical supports, an ensemble of particle structures should be expected. The findings presented here might have a direct impact on understanding the site-specific functionality of the technologically important catalytic material, Pt/CeO_2, and on its ageing behavior. Our time-resolved atomic-resolution imaging approach outlines a straightforward experimental route to assess how substrate interactions affect the structure of supported nanoparticles. This approach, based on scanning transmission electron microscopy, is extendible to measurements in gas atmospheres under variable temperature conditions.

Data availability

Raw microscopy data and relaxed atomic models are available on figshare: **https://figshare.com/s/b269ca52beb834f496cd**.

Author contributions

H. E. acquired the microscopy data, analyzed it, and generated atomic models from it. Y. N. and R. E. P. deposited the Pt particles. H. G. performed the DFT calculations. R.E initiated and supervised the work. All authors have contributed to the preparation of the manuscript and given approval to the final version of the manuscript.

Conflicts of interest

There are no conflicts to declare.

Acknowledgements

H. E. and R. E. acknowledge funding from the Swiss National Science Foundation (200021_196381). H. G. acknowledges funding from the Swedish Research Council (2020-05191) and computational time through a SNIC grant. R. E. P. and Y. N. thank the Welsh Government for their financial support.

References

1 J. M. Rahm and P. Erhart, *Nano Lett.*, 2017, **17**, 5775–5781.
2 C. R. Henry, *Prog. Surf. Sci.*, 2005, **80**, 92–116.
3 T. W. van Deelen, C. Hernández Mejía and K. P. de Jong, *Nat. Catal.*, 2019, **2**, 955–970.
4 N. Shibata, A. Goto, K. Matsunaga, T. Mizoguchi, S. D. Findlay, T. Yamamoto and Y. Ikuhara, *Phys. Rev. Lett.*, 2009, **102**, 136105.
5 P. L. Hansen, J. B. Wagner, S. Helveg, J. R. Rostrup-Nielsen, B. S. Clausen and H. Topsøe, *Science*, 2002, **295**, 2053–2055.
6 H. Frey, A. Beck, X. Huang, J. A. van Bokhoven and M. G. Willinger, *Science*, 2022, **376**, 982–987.
7 Y. He, J.-C. Liu, L. Luo, Y.-G. Wang, J. Zhu, Y. Du, J. Li, S. X. Mao and C. Wang, *Proc. Natl. Acad. Sci. U. S. A.*, 2018, **115**, 7700–7705.
8 J. L. Vincent and P. A. Crozier, *Nat. Commun.*, 2021, **12**, 5789.
9 T. Akita, S. Tanaka, K. Tanaka and M. Kohyama, *Mater. Sci. Forum*, 2010, **654–656**, 2362–2365.
10 T. Nilsson Pingel, M. Jørgensen, A. B. Yankovich, H. Grönbeck and E. Olsson, *Nat. Commun.*, 2018, **9**, 2722.
11 Z. Tang, I. Surin, A. Rasmussen, F. Krumeich, E. V. Kondratenko, V. A. Kondratenko and J. Pérez-Ramírez, *Angew. Chem., Int. Ed.*, 2022, **61**, e202200772.
12 P. D. Nellist and S. J. Pennycook, *Science*, 1996, **274**, 413–415.
13 F. J. Caparrós, L. Soler, M. D. Rossell, I. Angurell, L. Piccolo, O. Rossell and J. Llorca, *ChemCatChem*, 2018, **10**, 2365–2369.
14 T. R. Henninen, M. Bon, F. Wang, D. Passerone and R. Erni, *Angew. Chem., Int. Ed.*, 2020, **59**, 839–845.
15 R. Erni, M. D. Rossell, C. Kisielowski and U. Dahmen, *Phys. Rev. Lett.*, 2009, **102**, 096101.
16 S. Van Aert, K. J. Batenburg, M. D. Rossell, R. Erni and G. Van Tendeloo, *Nature*, 2011, **470**, 374–377.

17 S. Bals, M. Casavola, M. A. van Huis, S. Van Aert, K. J. Batenburg, G. Van Tendeloo and D. Vanmaekelbergh, *Nano Lett.*, 2011, **11**, 3420–3424.
18 R. Xu, C.-C. Chen, L. Wu, M. C. Scott, W. Theis, C. Ophus, M. Bartels, Y. Yang, H. Ramezani-Dakhel, M. R. Sawaya, H. Heinz, L. D. Marks, P. Ercius and J. Miao, *Nat. Mater.*, 2015, **14**, 1099–1103.
19 R. Ishikawa, A. R. Lupini, Y. Hinuma and S. J. Pennycook, *Ultramicroscopy*, 2015, **151**, 122–129.
20 A. De Backer, G. T. Martinez, A. Rosenauer and S. Van Aert, *Ultramicroscopy*, 2013, **134**, 23–33.
21 Z. Y. Li, N. P. Young, M. Di Vece, S. Palomba, R. E. Palmer, A. L. Bleloch, B. C. Curley, R. L. Johnston, J. Jiang and J. Yuan, *Nature*, 2008, **451**, 46–48.
22 R. Erni, H. Heinrich and G. Kostorz, *Ultramicroscopy*, 2003, **94**, 125–133.
23 E. J. Kirkland, R. F. Loane and J. Silcox, *Ultramicroscopy*, 1987, **23**, 77–96.
24 J. M. LeBeau, S. D. Findlay, L. J. Allen and S. Stemmer, *Nano Lett.*, 2010, **10**, 4405–4408.
25 J. M. LeBeau, S. D. Findlay, L. J. Allen and S. Stemmer, *Phys. Rev. Lett.*, 2008, **100**, 206101.
26 L. Nie, D. Mei, H. Xiong, B. Peng, Z. Ren, X. I. P. Hernandez, A. DeLaRiva, M. Wang, M. H. Engelhard, L. Kovarik, A. K. Datye and Y. Wang, *Science*, 2017, **358**, 1419–1423.
27 S. Lee, J. Seo and W. Jung, *Nanoscale*, 2016, **8**, 10219–10228.
28 S. Xie, L. Liu, Y. Lu, C. Wang, S. Cao, W. Diao, J. Deng, W. Tan, L. Ma, S. N. Ehrlich, Y. Li, Y. Zhang, K. Ye, H. Xin, M. Flytzani-Stephanopoulos and F. Liu, *J. Am. Chem. Soc.*, 2022, **144**, 21255–21266.
29 K. Ding, A. Gulec, A. M. Johnson, N. M. Schweitzer, G. D. Stucky, L. D. Marks and P. C. Stair, *Science*, 2015, **350**, 189–192.
30 N. Daelman, M. Capdevila-Cortada and N. López, *Nat. Mater.*, 2019, **18**, 1215–1221.
31 F. Maurer, J. Jelic, J. Wang, A. Gänzler, P. Dolcet, C. Wöll, Y. Wang, F. Studt, M. Casapu and J.-D. Grunwaldt, *Nat. Catal.*, 2020, **3**, 824–833.
32 A. I. Boronin, E. M. Slavinskaya, A. Figueroba, A. I. Stadnichenko, T. Y. Kardash, O. A. Stonkus, E. A. Fedorova, V. V. Muravev, V. A. Svetlichnyi, A. Bruix and K. M. Neyman, *Appl. Catal., B*, 2021, **286**, 119931.
33 H. Wang, J.-X. Liu, L. F. Allard, S. Lee, J. Liu, H. Li, J. Wang, J. Wang, S. H. Oh, W. Li, M. Flytzani-Stephanopoulos, M. Shen, B. R. Goldsmith and M. Yang, *Nat. Commun.*, 2019, **10**, 3808.
34 H. Xiong, D. Kunwar, D. Jiang, C. E. García-Vargas, H. Li, C. Du, G. Canning, X. I. Pereira-Hernandez, Q. Wan, S. Lin, S. C. Purdy, J. T. Miller, K. Leung, S. S. Chou, H. H. Brongersma, R. ter Veen, J. Huang, H. Guo, Y. Wang and A. K. Datye, *Nat. Catal.*, 2021, **4**, 830–839.
35 G. Ferré, M. Aouine, F. Bosselet, L. Burel, F. J. Cadete Santos Aires, C. Geantet, S. Ntais, F. Maurer, M. Casapu, J. D. Grunwaldt, T. Epicier, S. Loridant and P. Vernoux, *Catal. Sci. Technol.*, 2020, **10**, 3904–3917.
36 T. Tong, M. Douthwaite, L. Chen, R. Engel, M. B. Conway, W. Guo, X.-P. Wu, X.-Q. Gong, Y. Wang, D. J. Morgan, T. Davies, C. J. Kiely, L. Chen, X. Liu and G. J. Hutchings, *ACS Catal.*, 2023, **13**, 1207–1220.
37 J. Wang, E. Sauter, A. Nefedov, S. Heißler, F. Maurer, M. Casapu, J.-D. Grunwaldt, Y. Wang and C. Wöll, *J. Phys. Chem. C*, 2022, **126**, 9051–9058.
38 N. Bosio, M. Di, M. Skoglundh, P.-A. Carlsson and H. Grönbeck, *J. Phys. Chem. C*, 2022, **126**, 16164–16171.
39 N. V. Skorodumova, M. Baudin and K. Hermansson, *Phys. Rev. B: Condens. Matter Mater. Phys.*, 2004, **69**, 075401.
40 S. Yoon, H. Ha, J. Kim, E. Nam, M. Yoo, B. Jeong, H. Y. Kim and K. An, *J. Mater. Chem. A*, 2021, **9**, 26381–26390.
41 B. Song, D. Choi, Y. Xin, C. R. Bowers and H. Hagelin-Weaver, *Angew. Chem., Int. Ed.*, 2021, **60**, 4038–4042.
42 S. Pratontep, S. J. Carroll, C. Xirouchaki, M. Streun and R. E. Palmer, *Rev. Sci. Instrum.*, 2005, **76**, 045103.
43 R. Tran, Z. Xu, B. Radhakrishnan, D. Winston, W. Sun, K. A. Persson and S. P. Ong, *Sci. Data*, 2016, **3**, 160080.
44 J. Liu, *ChemCatChem*, 2011, **3**, 934–948.
45 Y. Lykhach, S. M. Kozlov, T. Skála, A. Tovt, V. Stetsovych, N. Tsud, F. Dvořák, V. Johánek, A. Neitzel, J. Mysliveček, S. Fabris, V. Matolín, K. M. Neyman and J. Libuda, *Nat. Mater.*, 2016, **15**, 284–288.
46 M. Capdevila-Cortada and N. López, *Nat. Mater.*, 2017, **16**, 328–334.
47 D. B. Williams and C. B. Carter, in *Transmission Electron Microscopy: A Textbook for Materials Science*, Springer US, Boston, MA, 2009, pp. 53–71, DOI: **10.1007/978-0-387-76501-3_4**.
48 L. Jones, H. Yang, T. J. Pennycook, M. S. J. Marshall, S. Van Aert, N. D. Browning, M. R. Castell and P. D. Nellist, *Adv. Struct. Chem. Imaging*, 2015, **1**, 8.
49 A. De Backer, K. H. W. van den Bos, W. Van den Broek, J. Sijbers and S. Van Aert, *Ultramicroscopy*, 2016, **171**, 104–116.
50 J. Barthel, *Ultramicroscopy*, 2018, **193**, 1–11.
51 G. Kresse and J. Hafner, *Phys. Rev. B: Condens. Matter Mater. Phys.*, 1993, **47**, 558–561.
52 G. Kresse and J. Furthmüller, *Comput. Mater. Sci.*, 1996, **6**, 15–50.
53 G. Kresse and J. Furthmüller, *Phys. Rev. B: Condens. Matter Mater. Phys.*, 1996, **54**, 11169–11186.
54 P. E. Blöchl, *Phys. Rev. B: Condens. Matter Mater. Phys.*, 1994, **50**, 17953–17979.
55 J. P. Perdew, K. Burke and M. Ernzerhof, *Phys. Rev. Lett.*, 1996, **77**, 3865–3868.
56 V. I. Anisimov, J. Zaanen and O. K. Andersen, *Phys. Rev. B: Condens. Matter Mater. Phys.*, 1991, **44**, 943–954.
57 M. Huang and S. Fabris, *J. Phys. Chem. C*, 2008, **112**, 8643–8648.
58 W. Tang, E. Sanville and G. Henkelman, *J. Phys.: Condens. Matter*, 2009, **21**, 084204.